Electronic and transport properties of the Te-defect lattice in $DyTe_{1.8}$

Jinwoong Kim* and Nicholas Kioussis†
Department of Physics and Astronomy, California State University, Northridge, California 91330, USA

(Received 2 July 2024; revised 13 November 2024; accepted 14 November 2024; published 2 December 2024)

The rare-earth ditellurides are known to form a two-dimensional square lattice where the strong Fermi surface nesting leads to structural modulation. In contrast to charge density waves, the supercell modulation is accompanied by the formation of the periodic Te vacancy network, where the Te deficiency affects the nesting vector, i.e., the supercell size, via tuning the chemical potential. In this work, first-principles electronic-structure calculations for the $\sqrt{5} \times \sqrt{5}$ supercell, which commonly appears in this family of tellurides, reveal interesting electronic and transport properties of the Te defect lattice in $DyTe_{1.8}$. The reconstruction of the Te-deficient square lattice, consisting of a single Te dimer and a pair of Te trimers per unit cell, gives rise to an out-of-plane polarization, whose direction depends on the position of the dimer. This results in various close-in-energy parallel and antiparallel polarization configurations of successive Te layers depending on the dimer positions. We predict that the orientation of the Te dimers, and hence the corresponding structural motifs, can be reversibly switched between two in-plane perpendicular directions under tensile epitaxial strain via a piezoelectric substrate, resulting in a colossal conductivity switching. Furthermore, the Te-dimer orientations result in an asymmetric Fermi surface, which can be confirmed by quantum oscillations measurements.

DOI: 10.1103/PhysRevB.110.245106

I. INTRODUCTION

The rare-earth ditellurides RTe_2 (R represents a lanthanide element) are a family of layered materials renowned for a wide range of intriguing properties at low temperature. These include charge density waves (CDWs) [1,2] magnetism [3], superconductivity under high pressure [4], and the simultaneous presence of a CDW, superconductivity, and antiferromagnetism [1]. The unit cell of the crystal structure comprises double-corrugated R-Te quasi-ionic layers separated by single planar square Te sheets stacked in the [001] direction, as illustrated in Fig. 1(a). From the electronic-structure point of view, each $(R\text{-Te})^{1+}$ pair on the corrugated layer donates one electron to the Te atoms (Te_s) in the square plane [5,6].

In contrast to the rare-earth tritellurides RTe_3, which form stoichiometric compounds, the $RTe_{2-\delta}$ ($0.0 \lesssim \delta \lesssim 0.2$) compounds host Te_s vacancies on the Te_s square layer, giving rise to a wide range of structural motifs which depends sensitively on the Te deficiency δ and the rare-earth cation [7,8]. The Te_s vacancies effectively contribute extra charge to the layer which, along with the isolated Te^{2-} anions, forms differently ordered patterns within the Te sheets. This results in superstructure modulations which can be commensurate with the parent structure, such as in $CeSe_{1.9}$ [9] and Gd_8Se_{15} [10] structures, and incommensurate modulated structures, such as $DySe_{1.84}$ [11] and $RSe_{1.84}$ (R = La–Nd, Sm) [12].

Recently, we reported [7] experimental and first-principles electronic-structure studies of the supercell formation in epitaxial $DyTe_{2-\delta}$ thin films, where for $\delta = 0.2$ the modulation is a $(\sqrt{5} \times \sqrt{5})$ R26.6° $\times 2$ superlattice. The superlattice emerges due to a periodic Te-defect lattice, which also acts to open a gap in the electronic spectrum and induces semiconducting transport behavior. First-principles calculations point towards nesting conditions of the Fermi surface at a $\boldsymbol{q}$ vector that corresponds to the $\sqrt{5} \times \sqrt{5}$ condition, suggesting that the formation of the defect lattice results from a driving force similar to the conventional picture of CDW formation, where sections of the Fermi surface are gapped out by the formation of supercells with periodicity corresponding to the nesting condition [13]. Our total energy calculations [7] of the $\sqrt{5} \times \sqrt{5}$ supercell with Te_s mono- and divacancies in different configurations for $\delta = 0.1$ and 0.2 showed that the second-nearest-neighbor vacancy configuration [referred to as the A-C configuration in Fig. 5(c) of Ref. [7]] has the lowest formation energy among the various structures considered, in agreement with previous x-ray-diffraction measurements in $SmTe_{1.8}$ [14]. The second-nearest-neighbor divacancy configuration shown in Fig. 2(c), where the divacancies nucleate on sites 0 and 4 {0, 4} in Fig. 2(a), consists of an ordered lattice of Te_s dimers and trimers. Furthermore, first-principles calculations of the $(\sqrt{5} \times \sqrt{5}) \times 2$ modulation along the c axis corresponding to the nucleation of a pair of A-C (0,4) divacancies on two Te square layers reveal that the second-nearest-neighbor A-C divacancy appears at a laterally displaced position (0.5, 0.5) relative to the divacancy on the adjacent Te square net layer [7].

The objective of this work is to reveal the emergence of interesting properties of the periodic Te-defect lattice associated with the onset of ferroelectric polarization, which depends sensitively on the position of the Te dimer. In Sec. II we outline the methodology employed. In Sec. III we present results of the position and orientation of the various Te-dimer configurations (Sec. III A), the potential arrangement of dimer

*Contact author: jinwoong.kim@csun.edu
†Contact author: nick.kioussis@csun.edu

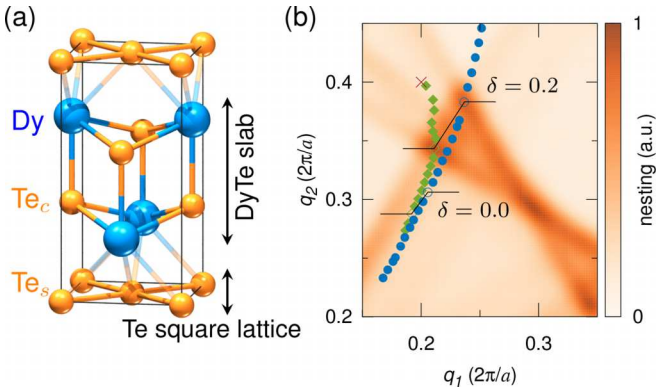

FIG. 1. (a) Unit cell of pristine $DyTe_2$ with two Te sites Te_s on the square net layer. (b) Calculated nesting function of $DyTe_2$. The background color map illustrates the Gaussian-smeared nesting function for an electron doping level corresponding to Te deficiency, $\delta = 0.2$. The red cross at (0.2,0.4) indicates the $\sqrt{5} \times \sqrt{5}$ wave vector. The two local nesting function peaks are marked with dots upon the doping level, which moves away from the origin with increasing electron doping.

orientations (Sec. III B), the polarization coupled with the dimer position (Sec. III C), the density of states with divergent peaks (Sec. III D), the Fermi surface anisotropy (Sec. III E), and the transport properties (Sec. III F). Conclusions are summarized in Sec. IV.

II. METHODOLOGY

The density functional theory calculations are performed using the Vienna *ab initio* simulation package [15,16] with the projector augmented wave method [17,18]. The Dy $4f$ states are treated as a core with valence configurations $5p^6 5d^1 6s^2$ and $5s^2 5p^4$ for Te. All structures are optimized using the PBEsol exchange-correlation functional [19] and the Bloch states are calculated and wannierized [20,21] with the a modified Becke-Johnson potential [22,23], which provides accurate band gaps, effective masses, and frontier-band ordering. The momentum space is sampled at a $80 \times 80 \times 80k$-point mesh with the Wannier interpolation scheme. The conductivity is calculated using the semiclassical Boltzmann transport theory assuming a constant relaxation time. The tetrahedron method is employed to obtain the Fermi surface and its cross-section area. In the polarization calculation, the topmost 51 valence bands are wannierized for each spin channel where three and two p orbitals are initially projected on the Te_c and Te_s atoms, respectively, and five s orbitals are projected at the center of the Te-Te bonds in the square lattice. The integer ionic charges Z_n in Eq. (6) are $+3$ for Dy and $+4$ for Te atoms.

III. RESULTS AND DISCUSSION

A. Crystal structure

The crystal structure of pristine $DyTe_2$ is shown in Fig. 1(a), where the buckled DyTe slabs are separated by the planar Te square lattice that tends to undergo a supercell modulation whose periodicity interestingly depends on the Te vacancy concentration [7,8]. The nesting function $N(\boldsymbol{q})$ of the Fermi surface for an electron doping corresponding

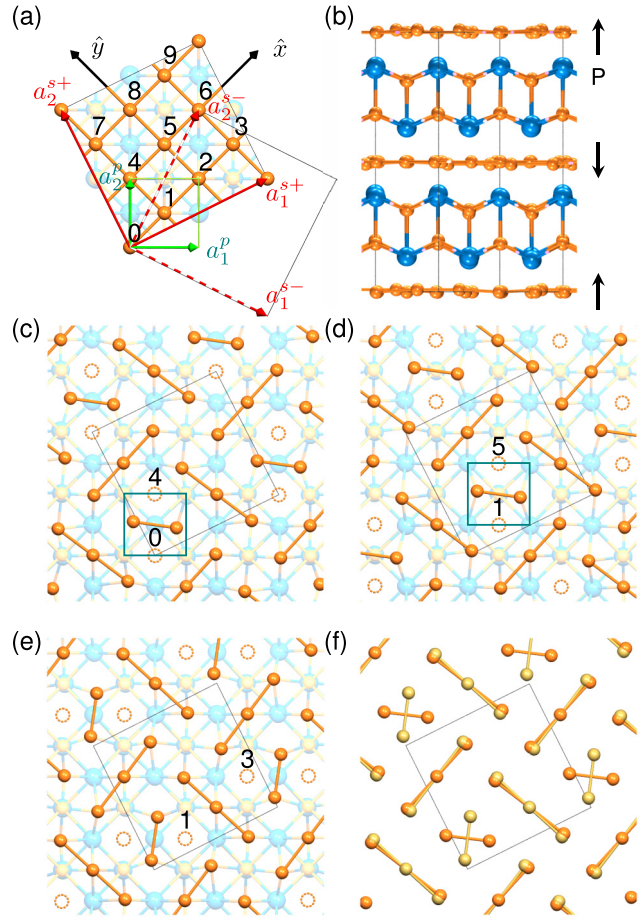

FIG. 2. Structural modulation of $DyTe_2$. (a) Projection of the Te square network on the (001) plane, where the numerical indices of the $\sqrt{5} \times \sqrt{5}$ modulated cell denote the plausible positions of the Te_s divacancies. The $\boldsymbol{a}_i^p$ are the primitive lattice vectors and $\boldsymbol{a}_i^{s\pm}$ are two sets of supercell lattice vectors with $\pm$ chirality. (b) Side view of $\sqrt{5} \times \sqrt{5} \times 2$ modulated $DyTe_{1.8}$. Arrows depict the polarization configuration of individual Te square lattice layers in the ground state. The reconstructed ordered Te square network of $DyTe_{1.8}$ is shown for several Te divacancy positions and orientations at the (c) $\{0, 4\}$, (d) $\{1, 5\}$, and (e) $\{1, 3\}$ sites. Small squares in (c) and (d) denote the pristine cell enclosing the Te dimer. (f) Mixed phase of the reconstructed Te square network comprised of the structural motifs of (c) and (e), respectively, where the large square denotes the $\sqrt{5} \times \sqrt{5}$ cell.

to the Te deficiency $\delta = 0.2$, reported in our recent calculations [Fig. S7(h) in the supporting information of Ref. [7]], is replotted in Fig. 1(b), which shows a close-up near the $\boldsymbol{q}$ point corresponding to the $\sqrt{5} \times \sqrt{5}$ modulation, marked with a cross at (0.2,0.4). Two strong peaks near the cross, illustrated with dark orange colors, are traced as a function of doping, displayed with the blue and green dots, where their separation increases with electron doping. The green peak is found to pass the cross at a higher Te deficient level ($\delta > 0.2$) that does not necessarily imply the need for additional Te vacancies, since the nesting function calculations involve several assumptions such as the rigid band approximation, constant matrix elements, and the exclusion of strain effect on the chemical potential. Our calculations demonstrate

that the nesting function peaks associated with the formation of various supercell modulations change with chemical doping. In particular, the nesting function peaks (denoted by blue and green dots) approach the $\sqrt{5}\times\sqrt{5}$ modulation $\boldsymbol{q}$ vectors with increasing Te deficiency, in good agreement with experiments.

Consequently, in this work we focus on the $\sqrt{5}\times\sqrt{5}$ modulation that commonly occurs for various rare-earth elements with two Te_s vacancies per modulated cell ($\delta = 0.2$) [7]. The in-plane lattice vectors of the supercell exhibiting chirality, shown in Fig. 2(a), are

$$\begin{aligned} \boldsymbol{a}_1^p &= \frac{a_0}{\sqrt{2}}(\hat{x}-\hat{y}), \quad \boldsymbol{a}_2^p = \frac{a_0}{\sqrt{2}}(\hat{x}+\hat{y}), \\ \boldsymbol{a}_1^{s\pm} &= 2\boldsymbol{a}_1^p \pm \boldsymbol{a}_2^p, \quad \boldsymbol{a}_2^{s\pm} = \mp\boldsymbol{a}_1^p + 2\boldsymbol{a}_2^p, \end{aligned} \tag{1}$$

where $\boldsymbol{a}_i^p$ are the primitive lattice vectors and $\boldsymbol{a}_i^{s\pm}$ are two sets of supercell lattice vectors with $\pm$ chirality. In general, a synthesized sample may have both types of domains leading to domain walls across which the chirality gets reversed. The two supercell structures with different chirality and their physical properties can be transformed to each other by a mirror operator $\mathcal{M}_y : (x, y, z) \to (x, -y, z)$. Unless stated otherwise, throughout the remainder of this paper we focus on only the $+$ chirality structure and ignore for convenience the superscript $s+$, namely, $\boldsymbol{a}_i \equiv \boldsymbol{a}_i^{s+}$.

The numerical indices in Fig. 2(a) represent the ten Te_s sites of the $\sqrt{5}\times\sqrt{5}$ supercell where the divacancy may be placed. The second-nearest-neighbor divacancy (such as $\{0, 4\}$, referred to as the A-C configuration in Ref. [7]) is found to have the lowest formation energy for the $\sqrt{5}\times\sqrt{5}$ modulation. The reconstructed square lattice consists of one Te dimer and two Te trimers per unit cell, resulting in several isoenergetic and ordered structural motifs. Figures 2(c) and 2(d) show the first and second structural motifs, associated with the $\{0, 4\}$ and $\{1, 5\}$ second-nearest-neighbor divacancies, respectively, that look almost identical except for their positions relative to the DyTe slab. The thick squares in each panel emphasize the position of the Te_s dimers whose centers lie atop the Dy (Te_c) atoms for the first (second) structural motif. The two structural motifs transform into each other through the mirror operation $\mathcal{M}_z$, followed by a proper in-plane translation, indicating a finite vertical polarization whose sign depends on the position of the Te dimer, as will be discussed in the next section. The divacancy also reduces the $\mathcal{C}_4$ rotation symmetry of the pristine supercell to the $\mathcal{C}_2$ symmetry, whose rotational axis can be placed at the center of the Te dimer. The third structural motif associated with the $\{1, 3\}$ divacancy can be transformed into the first motif of the $\{0, 4\}$ divacancy through a $\mathcal{C}_4$ rotation, as illustrated in Figs. 2(c) and 2(e). In general, CDWs with a commensurate cell modulation of $n \times m$ can introduce nm distinct types of domains, associated with the relative translations of the modulated supercell. Therefore, there can be five different types of domains for the $\sqrt{5}\times\sqrt{5}$ modulation of $\mathrm{DyTe}_{1.8}$. It is noteworthy that the three structural motifs discussed above do not transform into one another via lateral translation alone. The total number of distinct domains amounts to $2 \times 2 \times 5 = 20$, where the first (second) factor of 2 arises from the two possible positions (orientations) of the Te dimer in addition to the factor of 5 due to the lateral translations.

B. Dimer orientation arrangement

The actual $\mathrm{DyTe}_{1.8}$ samples may consist of a mixed phase of the $\{0, 4\}$- and $\{1, 3\}$-based structural motifs as shown in Fig. 2(f). This in turn raises an intriguing question whether the orientation of the Te dimers, corresponding to the two isoenergetic structural motifs, can be aligned. In order to understand the potential dimer-orientation ordering, we consider dimer-dimer couplings and dimer-strain couplings.

The dimer-dimer coupling energy up to the second-nearest neighbor can be written as

$$E_{\mathrm{coupling}} = \Lambda_1 \nu_1 + \Lambda_2 \nu_2, \tag{2}$$

where Λ_1 and Λ_2 are the first- and second-nearest coupling energies, respectively, and ν_i are the sums of the mutual-dimer-orientation-coupling variables that run over all the first- ($i = 1$) and second- ($i = 2$) nearest-neighbor sites, namely,

$$\nu_1 = \sum_{\langle i,j\rangle} c_i c_j, \quad \nu_2 = \sum_{\langle\langle i,j\rangle\rangle} c_i c_j. \tag{3}$$

Here $c_n = \pm 1$ denotes either of the dimer orientations. The single and double angular brackets indicate the first- and second-nearest-neighbor pairs, respectively. Figures 3(a)–3(d) show four different dimer-orientation configurations whose coupling parameters (ν_1, ν_2) are given in the caption. The structures are relaxed with fixed in-plane lattice vectors so that all structures preserve tetragonal symmetry. By fitting the total energies, we find that the coupling energies are

$$\Lambda_1 \simeq 5\ \mathrm{meV}, \quad \Lambda_2 \simeq 6\ \mathrm{meV}. \tag{4}$$

Positive values indicate that dimer orientations of opposite sign are favored at neighbor sites. The coupling of the first-nearest neighbor is slightly weaker than that of the second-nearest neighbor, leading to a stripe pattern [i.e., periodic repetition of Fig. 3(d)] of the ground state. However, the estimated coupling energies are negligibly small compared to the synthesizing temperatures [7,8], indicating a random distribution of the dimer orientations. This raises the interesting question whether the stripe pattern can be synthesized via a slow cooling down after annealing so that the dimer configurations are not quenched.

Such a random distribution of the dimer orientation can then preserve the tetragonal symmetry in macroscopic scale while the microscopic local domains reduce the in-plane symmetry from C_4 to C_2, leading to a coupling between the dimer orientation and the in-plane strain. Figure 3(e) shows the landscape of the total energy difference $\Delta E = E(\{0, 4\}) - E(\{1, 3\})$ between the $\{0, 4\}$ and $\{1, 3\}$ divacancy structural motifs under in-plane strain, $r_x \equiv \frac{a_x}{a_0}$ and $r_y \equiv \frac{a_y}{a_0}$. Here a_0 is the in-plane equilibrium lattice constant from a tetragonal-symmetry-preserved calculation, and the relative directions of $\hat{x}$ and $\hat{y}$ to the supercell are shown in Fig. 2(a). The calculations reveal the dimer-strain coupling, showing that under 1% distortion, the energy difference exceeds 120 meV per Te dimer [Fig. 3(f)]. Hence, the sample may develop strain domains in which the dimers align according to the distortion of the domain. The neighbor domain would exhibit different lattice distortion to avoid the accumulation of stress. In this regard, the naturally grown samples can be considered as a

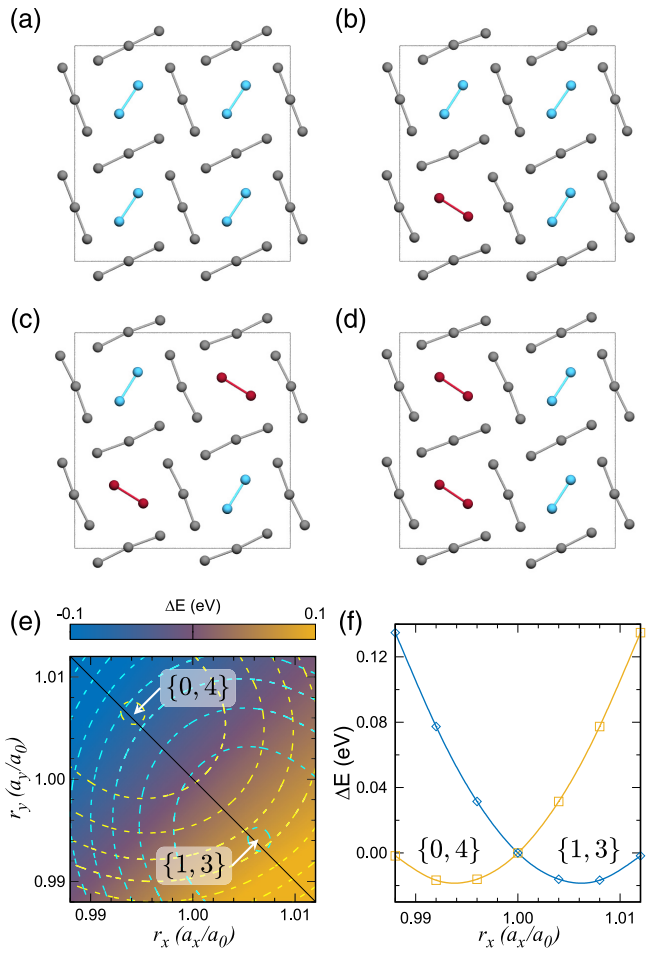

FIG. 3. Four different configurations of Te-dimer orientations in the $2\sqrt{5} \times 2\sqrt{5} \times 1$ supercell with coupling parameters (a) $(\nu_1, \nu_2) = (8, 8)$, (b) $(\nu_1, \nu_2) = (0, 0)$, (c) $(\nu_1, \nu_2) = (-8, 8)$, and (d) $(\nu_1, \nu_2) = (0, -8)$. The corrugated DyTe slabs are omitted from the figure for clarity. Red and blue colored dimers indicate positive ($c_i = +1$) and negative ($c_i = -1$) orientations, respectively. (e) Landscape of total energy difference $\Delta E = E(\{0, 4\}) - E(\{1, 3\})$ between the $\{0, 4\}$ and $\{1, 3\}$ divacancy structural motifs of the $\sqrt{5} \times \sqrt{5}$ supercell with two-dimensional epitaxial strain $r_x \equiv \frac{\alpha_x}{\alpha_0}$ and $r_y \equiv \frac{\alpha_y}{\alpha_0}$. Yellow and blue dashed curves indicate energy contours of the $\{0, 4\}$ and $\{1, 3\}$ phases, respectively. (f) Relative total energies of the two structural motifs under the in-plane lattice deformation along the black solid line shown in (e).

polycrystalline structure with different dimer orientations as well as lattice distortions. The relative domain sizes of either of the dimer orientations are then expected to depend on the epitaxial strain, providing an external knob to control the dimer-orientation ratio. (See the Supplemental Material [24] for the energy barrier of the dimer-rotation transition.) In the following sections, we discuss the electronic structure of a single domain, assuming that the dimer orientations are well aligned within the domain. Interestingly, as will be discussed below, these two distinct Te_s-vacancy ordered networks have substantial different transport properties.

C. Polarization

The emergence of the $\sqrt{5} \times \sqrt{5}$ superlattice induced by the periodic Te-vacant sites renders the $DyTe_{1.8}$ insulator [7]. The

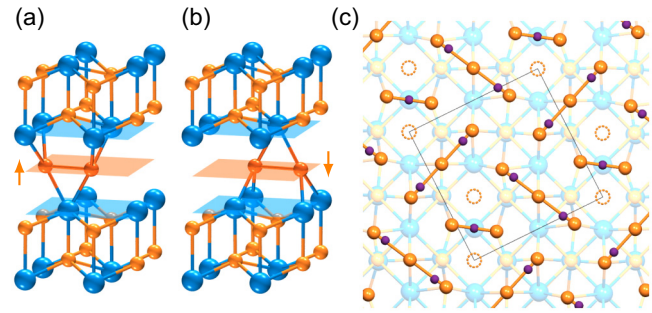

FIG. 4. Polarization of the Te square network. (a) Center of the Te dimer atop the Dy atom corresponding to the $\{0, 4\}$ divacancy configuration. (b) Center of the Te dimer atop the Te atom corresponding to the $\{1, 5\}$ divacancy configuration. The interlayer distances of the corrugated Dy-Te layers sandwiching the Te-dimer sheet are different. The Te trimers are omitted for clarity. (c) Wannier charge centers lying on the covalent bonds, denoted by the purple dots on the reconstructed Te square lattice for the $\{0, 4\}$ divacancy configuration. The position of the Wannier charge centers affects the polarization as well as the dipole moments.

formation of the divacancy breaks the inversion symmetry, which in turn results in finite polarization. Figures 4(a) and 4(b) clearly show the Dy-Te bonds of the Te_s dimers for the first and second structural motifs, which depend on their lateral position. More specifically, in the first motif, where the center of the Te dimer is atop the Dy atom, the dimer forms four (two) bonds with the Dy atoms on the upper (lower) layer, resulting in its proximity to the upper Dy-Te corrugated layer. Conversely, the second structural motif exhibits the opposite behavior.

The polarization $\boldsymbol{p}$ and dipole moment $\boldsymbol{d}$ of an insulator can be computed by considering the position of charged ions and Wannier charge centers (WCCs) of the occupied Bloch states below the insulating band gap [21,29]. As described in Sec. II, the topmost 51 valence bands, well separated from both the semicore states and the conduction bands, are wannierized. The Wannier functions are found exponentially localized near the initial position of projectors. Three and two Wannier functions are thus attached to Te_c and Te_s atoms, respectively. The positions of five interstitial Wannier functions, illustrated in Fig. 4(c), lie on the Te_s-Te_s bonds. The Wannier functions that deviate from the atomic sites render the system an obstructed atomic insulator [30–33]. The polarization and dipole moment are given by

$$\boldsymbol{d} = \boldsymbol{p}V \tag{5}$$

$$= Q_e\left(\sum_n^{\text{ions}} Z_n(\boldsymbol{R}_n - \boldsymbol{r}_0) - \sum_n^{\text{WCC}} D(\boldsymbol{r}_n - \boldsymbol{r}_0)\right) \tag{6}$$

$$= Q_e\left(\sum_n^{\text{ions}} Z_n\boldsymbol{R}_n - \sum_n^{\text{WCC}} D\boldsymbol{r}_n - \boldsymbol{r}_0\{N^+ - N^-\}\right) \tag{7}$$

$$= Q_e\left(\sum_n^{\text{ions}} Z_n\boldsymbol{R}_n - \sum_n^{\text{WCC}} D\boldsymbol{r}_n\right), \tag{8}$$

where V is the unit cell volume, Q_e is the electron charge, Z_n and $\boldsymbol{R}_n$ are the ionic charge number and atomic position of

TABLE I. Dipole moment and polarization of $DyTe_{1.8}$ for the $\{0, 4\}$ divacancy along the supercell lattice vectors $\boldsymbol{a}_i$ of the $\sqrt{5} \times \sqrt{5} \times 1$ cell.

$\boldsymbol{a}_i$	Dipole moment $Q_e\boldsymbol{a}_i$	Polarization (C/m^2)
$\boldsymbol{a}_1$	0.500	0.095
$\boldsymbol{a}_2$	0.500	0.095
$\boldsymbol{a}_3$	0.893	0.160

the nth atom, respectively, $\boldsymbol{r}_n$ is the position of the nth WCC, and $D = 2$ is the spin degeneracy of the Wannier functions. The origin $\boldsymbol{r}_0$ does not affect the dipole moment as it is charge neutral $N^+ = N^-$, where the net ionic charge $N^+ = \sum_n^{\text{ions}} Z_n$ is equal to the number of WCCs $N^- = D\sum_n^{\text{WCC}}$. Note that the WCC position $\boldsymbol{r}_n$ can be shifted by integer multiples of lattice vectors $\boldsymbol{r}_n \to \boldsymbol{r}_n + \sum_i m_i\boldsymbol{a}_i$ without affecting the physical observables that are associated with the gauge freedom, leading to the modulo definition of the modern theory of polarization [34–36]. The dipole moment is thus defined under modulo $DQ_e\boldsymbol{a}_i$ as long as the time-reversal symmetry is preserved on the surface as well as in the bulk.

The calculated dipole moment and polarization of the first structural motif of the $\{0, 4\}$ divacancy are listed in Table I. The $\mathcal{C}_2$ symmetry of the crystal structure confines the in-plane components of the dipole moments to be quantized [37] to either 0 or $\frac{1}{2}$ in units of $Q_e\boldsymbol{a}_{1,2}$. The calculated in-plane dipole moment value of $\frac{1}{2}$ indicates the nontrivial Zak phase [37] of $DyTe_{1.8}$ in the $\sqrt{5} \times \sqrt{5} \times 1$ supercell that induces metallic (side) surfaces due to the emergent in-gap states. We note that the physical samples, however, exhibit additional $\times 2$ structural modulation in the $\hat{z}$ direction [7], resulting in a $\sqrt{5} \times \sqrt{5} \times 2$ supercell which cancels out the in-plane dipole moment. The concept of quantized polarization under crystal symmetry was first elucidated by Zak [37] and subsequently integrated into the framework of topological insulators [35,38–40].

This additional modulation also controls the net dipole moment along the $\hat{z}$ direction as each layer may have an upward or a downward dipole moment depending on the position of the Te_s dimers of each layer. In our previous study [7], the total energy of the $\sqrt{5} \times \sqrt{5} \times 2$ supercell was calculated (see Table II) for various pairs of divacancy configurations $\{0, 4\} - \{d, d + 4\}$, $d = \{0, 1, 2, 3, 4, 5\}$, where the first divacancy nucleates at sites $\{0, 4\}$ on the first Te_s layer while the second pair nucleates on sites $\{d, d + 4\}$ on the second Te_s layer. The supercell structure with $d = 5$ is found to exhibit the lowest energy in which the polarization direction of the upper layer is opposite to that of the lower layer, as illustrated in Fig. 2(b). The next stable structure with $d = 2$ has 2.4 meV/Dy higher total energy and the polarization directions of the two layers are parallel, leading to finite net polarization, suggesting that an out-of-plane external electric field $E \gtrsim 15$ MV/m may stabilize the polarized structure.

TABLE II. Calculated total energy of the $\sqrt{5} \times \sqrt{5} \times 2$ supercell for the lateral position d of the divacancy on the second Te layer relative to the first. The relative polarization directions of the two layers are labeled as P and AP for parallel and antiparallel configurations, respectively.

	Displacement of second layer d					
Parameter	0	1	2	3	4	5
ΔE (meV/Dy)	0.0	−6.0	−8.4	−5.8	−7.3	−10.8
polarization	P	AP	P	AP	P	AP

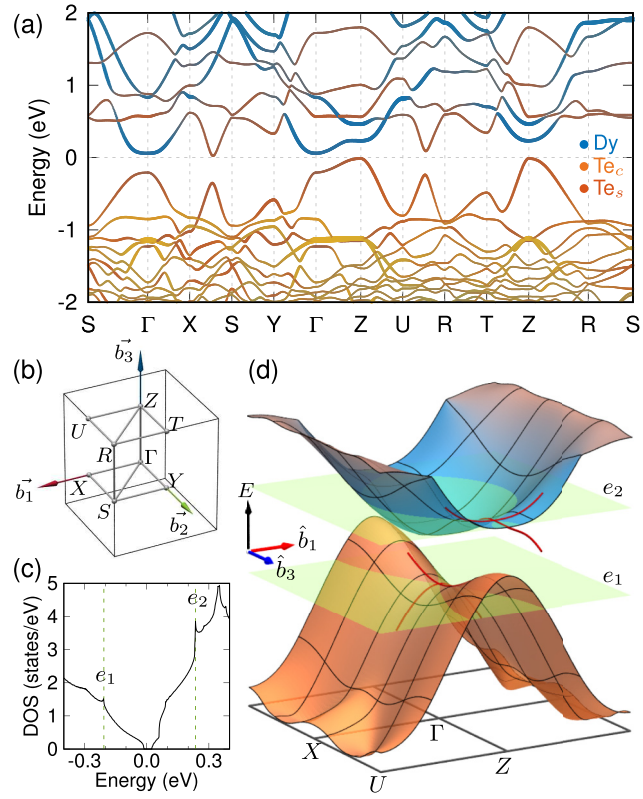

FIG. 5. Calculated electronic structure of $DyTe_{1.8}$ and Van Hove singularities near the Fermi level. (a) Band structure of the $\{0, 4\}$ divacancy configuration along high symmetry lines. (b) BZ of the $\sqrt{5} \times \sqrt{5}$ modulated supercell cell and the high-symmetry points, and Van Hove singularities near the Fermi level. (c) Calculated density of states near the Fermi level showing the emergence of Van Hove singularities at the energies e_1 and e_2 of the saddle points in both the hole- and electron-doped regimes. (d) Two-dimensional band structure on the $\hat{b}_1$-$\hat{b}_3$ plane, where the orange and blue colors denote the Te_s p and Dy d orbital characters, respectively. The valence (conduction) band exhibits a saddle point(s) at the Γ (near the Z) point marked with red curves. The energy levels e_1 and e_2 of the saddle points are illustrated with transparent planes.

D. Van Hove singularities

Figure 5 shows the calculated electronic structure of $DyTe_{1.8}$ with the $\{0, 4\}$ divacancy configuration. In Fig. 5(b) we plot the Brillouin zone (BZ) of the $\sqrt{5} \times \sqrt{5}$ modulated cell of $DyTe_{1.8}$ with the high-symmetry directions used in the band-structure plot. The blue, orange, and yellow colors denote projections on the Dy d, Te_s p, and Te_c p orbitals. Note that the Te_c-derived bands are well occupied below −0.9 eV

from the Fermi level and hardly affect the transport properties. The indirect (direct) band gap is 0.14 (0.33) eV, in qualitative agreement with the activation gap measured in transport [7].

In our previous study [7] of the electronic structure of pristine $DyTe_2$, we found that the Te_s p bands, originating from the square lattice, intersect the Fermi level and give rise to the nesting peaks near the $\boldsymbol{q}$ vectors corresponding to the $\sqrt{5} \times \sqrt{5}$ cell modulation. These nesting peaks explain the cell modulation and resulting insulating band gap in $DyTe_{1.8}$, which is further enhanced by the formation of the vacancy network, which increases the internested states' coupling strengths. The topmost valence band of $DyTe_{1.8}$ retains the two-dimensional (2D) nature of the square lattice, with highly dispersive bands along the in-plane direction and weakly dispersive bands along the out-of-plane direction such as the Γ-Z and R-S symmetry lines. The dimensional reduction in the band structure likely introduces saddle points, leading to Van Hove singularities (VHSs). Figure 5(d) illustrates the saddle points on the $\boldsymbol{b}_1$-$\boldsymbol{b}_3$ plane and the corresponding divergent peaks of the density of states. The conduction band, dominated by the Dy d orbital character, also exhibits saddle points on this plane which slightly deviate from the Z point by $\pm 0.1\boldsymbol{b}_3$. These VHSs in both the valence and conduction bands are expected to give rise to significant optical responses due to the high joint density of states, where the energy difference $e_2 - e_1 = 0.44$ eV corresponds to the infrared wavelength $\lambda = 2.8$ μm. However, these saddle points are separated in momentum space, necessitating a phonon coupling to complement the momentum difference $\Delta k_z \sim 0.4|\boldsymbol{b}_3|$. Fortunately, the system undergoes another double cell modulation along the $\hat{z}$ direction, which in turn folds the Z point to the Γ point. Thus, in the long-wavelength limit, optical absorption between the two saddle points can occur without phonon assistance. Additionally, the vertical polarization of each square lattice layer induces a Rashba spin splitting in the presence of spin-orbit coupling. The alignment of these layers' polarizations determines the spin texture chirality of the spin-split bands, influencing the band alignment and consequent optical responses. Further theoretical and experimental investigations are needed to fully understand these effects.

E. Fermi surface

Figures 6(a)–6(e) display the calculated 3D Fermi surface (FS) sheets and their (001) projections of $DyTe_{1.8}$ with the $\{0, 4\}$ divacancy configuration for chemical potential shifts $\mu = E - E_F$ ranging from $+0.3$ eV [Fig. 6(a)] to -0.5 eV [Fig. 6(e)] in steps of 0.2 eV. The orange and blue colors denote the Te_s p and Dy d orbital characters, respectively. For $\mu = -0.5$ eV the chemical potential lies in the Te_s p–derived valence bands [see Fig. 5(a)], and the FS consists of highly nested parallel sheets stacked normal to the Γ-S symmetry direction of the BZ [Fig. 5(b)]. As the chemical potential shifts upward in energy, the FS area gradually gets reduced and isolated pockets appear at the Z point. Above the Fermi level, two elongated electron pockets emerge on the side surface of the BZ as shown in Fig. 6(b) and eventually a Dy d–derived electron pocket emerges at the Γ point [Fig. 6(a)]. In Fig. 6(f) we display the FS sheets and their (001) projections for the $\{1, 3\}$ divacancy configuration for $\mu = -0.5$ eV. A comparison of Figs. 6(e) and 6(f) clearly shows the 90° rotation of the FS associated with the Te_s dimer rotation by 90° about [001], shown in Fig. 2(e). Since the group velocity is always normal to the FS, the parallel FS sheets indicate 1D conducting channels where their direction can be switched by the Te-dimer orientations, which will be discussed in the next section.

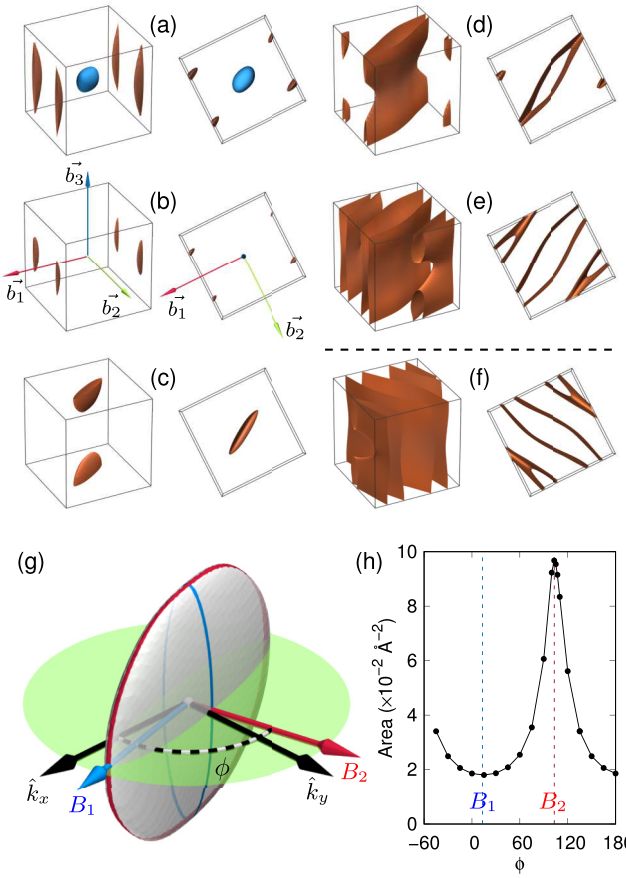

FIG. 6. Asymmetric Fermi surface sheets (left columns) and their (001) projections (right columns) of $DyTe_{1.8}$ with the $\{0, 4\}$ divacancy configuration for chemical potential shifts $\mu = E - E_F$ ranging from (a) $+0.3$ eV to (e) -0.5 eV in steps of 0.2 eV. Orange and blue colors denote the Te_s p and Dy d orbital characters, respectively. (f) FS sheets (left) and their (001) projections (right) for the $\{1, 3\}$ divacancy configuration for $\mu = -0.5$ eV. (g) Fermi surface at $\mu = -0.1$ eV. The green circular area shows the $\hat{k}_x$-$\hat{k}_y$ plane on which the external magnetic field is swept with an azimuthal angle ϕ from the $\hat{k}_x$ axis. The corresponding maximal cross-section paths under the external field along B_1 and B_2 are illustrated with blue and red stripes, respectively, on the Fermi surface. (h) Calculated maximal cross-section area versus ϕ.

As alluded to above, the valence bands are dominated by the Te_s atoms of the 2D square lattice. The Te-dimer orientations switch the hopping directions within the square lattice, which further refines the 2D-like band structure into an effective 1D channel, resulting in an asymmetric FS as shown in Fig. 6. The FS asymmetry can be confirmed by measuring the quantum oscillations under an external magnetic field whose frequency provides information about the maximal cross-section area of the FS. Figure 6(g) shows the disk-shape FS centered at the Z point under hole doping for $\mu = -0.1$ eV.

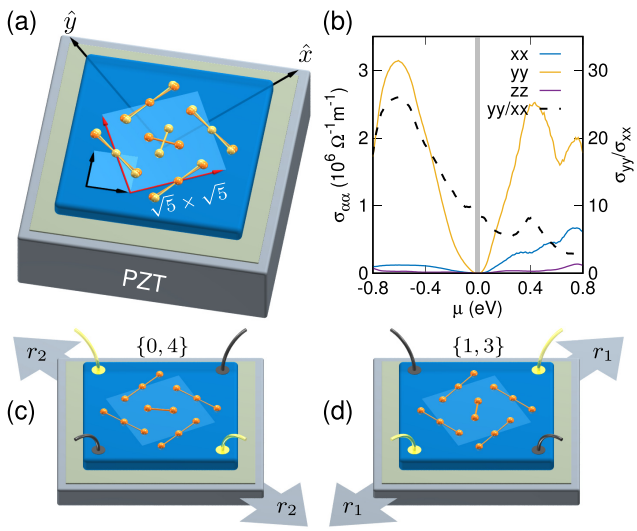

FIG. 7. Effect of uniaxial in-plane strain on Te-dimer orientation. (a) Schematic figure of $DyTe_{1.8}$ epitaxially grown on a piezoelectric substrate. Small (large) square shows the in-plane unit cell of a primitive $DyTe_2$ ($\sqrt{5} \times \sqrt{5}$ modulated $DyTe_{1.8}$) structure. (b) Calculated conductivity of $DyTe_{1.8}$ with the two vacancies at $\{0, 4\}$ versus the chemical potential μ. Conductivity along $\hat{y}$ [see (a) or Fig. 2(a) for the direction] is more than one order of magnitude higher compared to the other directions under hole doping. The dashed line denotes the in-plane conductivity ratio σ_{yy}/σ_{xx}. The band gap near $\mu = 0$ is marked with the gray box. (c) and (d) Relatively stable Te-dimer orientations under uniaxial strain. The (c) $\{0, 4\}$ and (d) $\{1, 3\}$ phases are preferred under uniaxial strain in the $\hat{y}$ and $\hat{x}$ directions, respectively. Gold (black) leads indicate the higher (lower) conductivity channel.

The maximal cross-section area shown in Fig. 6(h) is expected to strongly depend on the magnetic-field direction, where a peak appears at the azimuthal angle (measured from $\hat{k}_x$) $\phi \sim 103^\circ$, corresponding to B_2. The red stripe on the FS shows the cyclotron motion path under the external field B_2, while the blue stripe is under B_1, whose cross-section area is smaller than that of B_2 by a factor of 5.

F. Quasi-1D conducting channel

As discussed in Sec. III B, the in-plane strain couples to the dimer orientation, determining the orientation of the asymmetric FS as well [Figs. 6(e) and 6(f)]. Here we suggest an experimental setup to test the controllable anisotropic in-plane conductivity by using piezoelectric substrate as illustrated in Fig. 7(a). Regarding the release of the epitaxial strain with increasing film thickness [see Fig. 3(d) in Ref. [7]], this setup would be valid only for a thin-film device.

Figure 7(b) shows the matrix elements of the longitudinal conductivity σ_{ii} $(i = x, y, z)$ of $DyTe_{1.8}$ with the $\{0, 4\}$ divacancy configuration versus the chemical potential μ. The conductivity ratio $\frac{\sigma_{yy}}{\sigma_{xx}}$ versus μ is also plotted as a dashed line whose scale appears on the right vertical axis. Interestingly, σ_{yy} is higher by more than one order of magnitude compared to σ_{xx} under hole doping. This notable conductivity switching between the two phases upon the Te-dimer orientation suggests potential applications such as a memory device or a mechanical strain sensor. If the dimer orientations are fully aligned, one may reach a colossal conductivity contrast, ranging from 1000% to 2500% between the on and off phases.

Consequently, the Te dimer in the supercell acts as a molecular switch not only on a macroscopic scale but also on a microscopic level by controlling the electron hopping directions within the $\sqrt{5} \times \sqrt{5}$ supercell. This resembles the two-dimensional percolation network [41,42], where the overall conductivity is determined by the statistical configurations of the nanotube orientations. We acknowledge the significance of prior nanotube percolation experiments [43,44], particularly those where the nanotube orientation was controllable, which garnered considerable attention within the research community. Given the potential for strain-controlled dimer orientations, $DyTe_{1.8}$ emerges as another interesting platform to study the conductivity, determined by the statistical dimer-orientation configurations.

IV. SUMMARY

The structural and electronic properties of $DyTe_{1.8}$ were investigated by employing first-principles calculations. In addition to the $\sqrt{5} \times \sqrt{5}$ modulation, the detailed position and orientation of the Te dimers were found to play a crucial role in determining the polarization and the electronic structure near the Fermi level. The predicted small insulating gap with VHSs in both the valence and conduction bands imply characteristic optical responses with fine structures related to the polarization direction of each Te square lattice layer. The Te-dimer-orientation-induced asymmetric Fermi surface may be directly confirmed by quantum oscillation measurements and paves a way to memory device application with mechanically switchable quasi-one-dimensional conductivity. Our predictions of these interesting and diverse properties of $DyTe_{1.8}$ will hopefully motivate further experimental and theoretical investigations.

ACKNOWLEDGMENTS

We appreciate insightful discussions with Joseph Falson and Adrian Llanos. The work was supported by the NSF-PREP CSUN/Caltech-IQIM Partnership (Grant No. 2216774) and the NSF-Partnership in Research and Education in Materials (Grant No. DMR-1828019).

[1] K. Y. Shin, V. Brouet, N. Ru, Z. X. Shen, and I. R. Fisher, Electronic structure and charge-density wave formation in $LaTe_{1.95}$ and $CeTe_{2.00}$, Phys. Rev. B **72**, 085132 (2005).

[2] D. R. Garcia, G.-H. Gweon, S. Y. Zhou, J. Graf, C. M. Jozwiak, M. H. Jung, Y. S. Kwon, and A. Lanzara, Revealing charge density wave formation in the $LaTe_2$ system by angle

resolved photoemission spectroscopy, Phys. Rev. Lett. **98**, 166403 (2007).
[3] Y. Shin, C. Han, B. Min, H. Lee, C. Choi, Y. Kim, D. Kim, and Y. Kwon, Anisotropic magnetization in $R\mathrm{Te}_2$ (R: Ce, Pr, Gd and Sm), Physica B **291**, 225 (2000).
[4] M. H. Jung, A. Alsmadi, H. C. Kim, Y. Bang, K. H. Ahn, K. Umeo, A. H. Lacerda, H. Nakotte, H. C. Ri, and T. Takabatake, Superconductivity in magnetically ordered $\mathrm{CeTe}_{1.82}$, Phys. Rev. B **67**, 212504 (2003).
[5] W. Tremel and R. Hoffmann, Square nets of main-group elements in solid-state materials, J. Am. Chem. Soc. **109**, 124 (1987).
[6] A. Kikuchi, Electronic structure of lanthan ditellurides, J. Phys. Soc. Jpn. **67**, 1308 (1998).
[7] A. Llanos, S. Salmani-Rezaie, J. Kim, N. Kioussis, D. A. Muller, and J. Falson, Supercell formation in epitaxial rare-earth ditelluride thin films, Cryst. Growth Des. **24**, 115 (2024).
[8] H. Poddig, P. Gebauer, K. Finzel, K. Stöwe, and T. Doert, Structural variations and bonding analysis of the rare-earth metal tellurides $RE\mathrm{Te}_{1.875\pm\delta}$ (RE = Ce, Pr, Sm, Gd; $0.004 \leqslant \delta \leqslant 0.025$), Inorg. Chem. **60**, 11231 (2021).
[9] P. Plambeck-Fischer, W. Abriel, and W. Urland, Preparation and crystal structure of $RE\mathrm{Se}_{1.9}$ (RE = Ce, Pr), J. Solid State Chem. **78**, 164 (1989).
[10] E. Dashjav, O. Oeckler, T. Doert, H. Mattausch, and P. Böttcher, $\mathrm{Gd}_8\mathrm{Se}_{15}$—A 24-fold superstructure of the ZrSSi type, Angew. Chem., Int. Ed. **39**, 1987 (2000).
[11] A. van der Lee, L. M. Hoistad, M. Evain, B. J. Foran, and S. Lee, Resolution of the 66-fold superstructure of $\mathrm{DySe}_{1.84}$ by x-ray diffraction and second-moment scaled Hückel calculations, Chem. Mater. **9**, 218 (1997).
[12] C. Graf and T. Doert, $\mathrm{LaSe}_{1.85}$, $\mathrm{CeSe}_{1.83}$, $\mathrm{NdSe}_{1.83}$ and $\mathrm{SmSe}_{1.84}$–four new rare earth metal polyselenides with incommensurate site occupancy and displacive modulation, Z. Kristallogr. **224**, 568 (2009).
[13] S. Lee and B. J. Foran, Defective lattice charge density waves in $\mathrm{La}_{10}\mathrm{Se}_{19}$, $\mathrm{Cs}_3\mathrm{Te}_{22}$, $\mathrm{RbDy}_3\mathrm{Se}_8$, and $\mathrm{Dy}_{65.33}\mathrm{Se}_{120}$, J. Am. Chem. Soc. **118**, 9139 (1996).
[14] I. Ijjaali and J. A. Ibers, Two new binary lanthanide polytellurides: Syntheses and crystal structures of $\mathrm{CeTe}_{1.90}$ and $\mathrm{SmTe}_{1.80}$, J. Solid State Chem. **179**, 3456 (2006).
[15] G. Kresse and J. Furthmüller, Efficient iterative schemes for *ab initio* total-energy calculations using a plane-wave basis set, Phys. Rev. B **54**, 11169 (1996).
[16] G. Kresse and J. Furthmüller, Efficiency of *ab-initio* total energy calculations for metals and semiconductors using a plane-wave basis set, Comput. Mater. Sci. **6**, 15 (1996).
[17] P. E. Blöchl, Projector augmented-wave method, Phys. Rev. B **50**, 17953 (1994).
[18] G. Kresse and D. Joubert, From ultrasoft pseudopotentials to the projector augmented-wave method, Phys. Rev. B **59**, 1758 (1999).
[19] J. P. Perdew, A. Ruzsinszky, G. I. Csonka, O. A. Vydrov, G. E. Scuseria, L. A. Constantin, X. Zhou, and K. Burke, Restoring the density-gradient expansion for exchange in solids and surfaces, Phys. Rev. Lett. **100**, 136406 (2008).
[20] A. A. Mostofi, J. R. Yates, G. Pizzi, Y.-S. Lee, I. Souza, D. Vanderbilt, and N. Marzari, An updated version of wannier90: A tool for obtaining maximally-localised Wannier functions, Comput. Phys. Commun. **185**, 2309 (2014).
[21] N. Marzari, A. A. Mostofi, J. R. Yates, I. Souza, and D. Vanderbilt, Maximally localized Wannier functions: Theory and applications, Rev. Mod. Phys. **84**, 1419 (2012).
[22] A. D. Becke and E. R. Johnson, A simple effective potential for exchange, J. Chem. Phys. **124**, 221101 (2006).
[23] F. Tran and P. Blaha, Accurate band gaps of semiconductors and insulators with a semilocal exchange-correlation potential, Phys. Rev. Lett. **102**, 226401 (2009).
[24] See Supplemental Material at http://link.aps.org/supplemental/10.1103/PhysRevB.110.245106 for the calculated energy barrier of the dimer rotation, and which includes Refs. [25–28].
[25] G. Mills, H. Jónsson, and G. K. Schenter, Reversible work transition state theory: Application to dissociative adsorption of hydrogen, Surf. Sci. **324**, 305 (1995).
[26] H. Jónsson, G. Mills, and K. W. Jacobsen, in *Classical and Quantum Dynamics in Condensed Phase Simulations*, edited by B. J. Berne, G. Ciccotti, and D. F. Coker (World Scientific, Singapore, 1998), pp. 385–404.
[27] G. Henkelman, B. P. Uberuaga, and H. Jónsson, A climbing image nudged elastic band method for finding saddle points and minimum energy paths, J. Chem. Phys. **113**, 9901 (2000).
[28] G. Henkelman and H. Jónsson, Improved tangent estimate in the nudged elastic band method for finding minimum energy paths and saddle points, J. Chem. Phys. **113**, 9978 (2000).
[29] J. Kim, K. M. Rabe, and D. Vanderbilt, Negative piezoelectric response of van der Waals layered bismuth tellurohalides, Phys. Rev. B **100**, 104115 (2019).
[30] H. C. Po, H. Watanabe, and A. Vishwanath, Fragile topology and Wannier obstructions, Phys. Rev. Lett. **121**, 126402 (2018).
[31] S. K. Radha and W. R. L. Lambrecht, Topological obstructed atomic limit insulators by annihilating Dirac fermions, Phys. Rev. B **103**, 075435 (2021).
[32] X.-P. Li, D.-S. Ma, C.-C. Liu, Z.-M. Yu, and Y. Yao, From atomic semimetal to topological nontrivial insulator, Phys. Rev. B **105**, 165135 (2022).
[33] Y. Xu, L. Elcoro, Z.-D. Song, M. G. Vergniory, C. Felser, S. S. P. Parkin, N. Regnault, J. L. Mañes, and B. A. Bernevig, Filling-enforced obstructed atomic insulators, Phys. Rev. B **109**, 165139 (2024).
[34] R. D. King-Smith and D. Vanderbilt, Theory of polarization of crystalline solids, Phys. Rev. B **47**, 1651 (1993).
[35] D. Vanderbilt and R. D. King-Smith, Electric polarization as a bulk quantity and its relation to surface charge, Phys. Rev. B **48**, 4442 (1993).
[36] R. Resta, Macroscopic polarization in crystalline dielectrics: The geometric phase approach, Rev. Mod. Phys. **66**, 899 (1994).
[37] J. Zak, Berry's phase for energy bands in solids, Phys. Rev. Lett. **62**, 2747 (1989).
[38] Y. Aihara, M. Hirayama, and S. Murakami, Anomalous dielectric response in insulators with the π Zak phase, Phys. Rev. Res. **2**, 033224 (2020).
[39] M. Smeu, H. Guo, W. Ji, and R. A. Wolkow, Electronic properties of Si(111)-7 × 7 and related reconstructions: Density functional theory calculations, Phys. Rev. B **85**, 195315 (2012).
[40] J. Kim, C.-Y. Huang, H. Lin, D. Vanderbilt, and N. Kioussis, Bismuth antiphase domain wall: A three-dimensional

manifestation of the Su-Schrieffer-Heeger model, Phys. Rev. B **107**, 045135 (2023).

[41] M. Sahimi, *Application of Percolation Theory*, Applied Mathematical Sciences (Springer, Cham, 2023), Vol. 213.

[42] V. A. Cherkasova, Y. Y. Tarasevich, N. I. Lebovka, and N. V. Vygornitskii, Percolation of aligned dimers on a square lattice, Eur. Phys. J. B **74**, 205 (2010).

[43] F. Du, J. E. Fischer, and K. I. Winey, Effect of nanotube alignment on percolation conductivity in carbon nanotube/polymer composites, Phys. Rev. B **72**, 121404(R) (2005).

[44] C. Park, J. Wilkinson, S. Banda, Z. Ounaies, K. E. Wise, G. Sauti, P. T. Lillehei, and J. S. Harrison, Aligned single-wall carbon nanotube polymer composites using an electric field, J. Polym. Sci. B **44**, 1751 (2006).